2D and 3D Topology Optimization of a Heat-Exchanger Manifold for Flow Distribution in Laminar and Turbulent Regimes

Gupta, Mayank Kumar; Arnaud, Lionel; Hooman, Kamel

DOI
10.1080/01457632.2025.2578964

Publication date
2025

Document Version
Final published version

Published in
Heat Transfer Engineering

Heat Transfer Engineering

ISSN: 0145-7632 (Print) 1521-0537 (Online) Journal homepage: www.tandfonline.com/journals/uhte20

2D and 3D Topology Optimization of a Heat-Exchanger Manifold for Flow Distribution in Laminar and Turbulent Regimes

Mayank Kumar Gupta, Lionel Arnaud & Kamel Hooman

To cite this article: Mayank Kumar Gupta, Lionel Arnaud & Kamel Hooman (02 Nov 2025): 2D and 3D Topology Optimization of a Heat-Exchanger Manifold for Flow Distribution in Laminar and Turbulent Regimes, Heat Transfer Engineering, DOI: 10.1080/01457632.2025.2578964

To link to this article: https://doi.org/10.1080/01457632.2025.2578964

HEAT TRANSFER ENGINEERING
https://doi.org/10.1080/01457632.2025.2578964

Taylor & Francis
Taylor & Francis Group

2D and 3D Topology Optimization of a Heat-Exchanger Manifold for Flow Distribution in Laminar and Turbulent Regimes

Mayank Kumar Gupta[a], Lionel Arnaud[b], and Kamel Hooman[a]

[a]Process and Energy Department, Delft University of Technology, Delft, The Netherlands; [b]Laboratoire Génie de Production (LGP), Université de Technologie Tarbes Occitanie Pyrénées (UTTOP), Tarbes, France

ABSTRACT

Optimization of heat-exchanger manifolds can significantly improve the flow distribution inside their cores, improving the heat exchange and reducing flow obstruction. It also reduces the overall mass of the system and with it, the cost of additive manufacturing. However, during optimization, domains are typically modeled as 2D to minimize computing effort. Likewise, laminar flow is prescribed even when turbulence is expected in operation. The accuracy of such assumptions and their effect on optimized geometry is unclear. In this work, 2D topology optimization was first performed on an inlet manifold for both laminar and turbulent inlet boundary conditions. The resulting geometries were found to be starkly different, illustrating a difference in design concepts for different flow regimes. The laminar flow cases were then topology optimized with a 3D domain that modeled out-of-plane walls. This produced yet more different geometry, showing that these walls cannot be ignored. Experimental validation by testing stereolithography 3D prints proved that 3D optimization involves far more accurate flow modeling and the results are therefore likely to have better flow distribution.

Introduction

A variety of heat exchangers are used across multiple industries, ranging in size from multiple meters to submillimeter scales. All have the same objective: to transfer maximum possible heat from the source to the working fluid, with minimum wastage. In many contexts, however, additional concerns like size, weight, pumping losses, and cost also become extremely relevant. These must often be balanced with effective heat transfer, creating a major challenge for engineers.

The development of metal additive manufacturing (AM) techniques has pushed the envelope in heat exchanger design. One relevant family of techniques has been laser powder bed fusion. It involves laying powdered material in layers and fuzing parts of each layer *via* selective deposition of energy. Building in layers like this provides significantly greater freedom in part design than conventional subtractive techniques. The entire volume available can therefore now be optimized to meet an objective function with little to no consideration toward manufacturability. Performance achieved by these designs is therefore similar to conventional ones while requiring significantly lower pressure drop. Additionally, similar surface area can be packaged into much smaller volumes. Recognizing this, there has been significant work on designing such heat exchangers, especially for high performance applications like aviation [1] and supercritical power generation [2].

However, while a lot of attention has been given in literature to the design of the heat exchanger core, it has long been known that proper distribution of flow into the core is also critical. Work on plate-fin heat exchangers [3] and various other geometries [4] shows that maldistribution significantly reduces the thermal performance of a heat exchanger by creating hot spots and increasing the pressure drop [5]. Alongside performance concerns, an important metric for manifold design is the degree of compactness. Space-efficiency is not only desirable in its own right, but it also reduces overall heat exchanger volume and thus drops manufacturing cost significantly. It is therefore imperative that the manifold be optimized just as the core has been for AM.

CONTACT Professor Kamel Hooman k.hooman@tudelft.nl Process and Energy Department, Delft University of Technology, 2628 CB Delft, The Netherlands

Nomenclature

AM	additive manufacturing
c_{art}	artificial diffusion, m^2/s
CFD	computational fluid dynamics
d	width, mm
e	element size, mm
ED	energy dissipation, m^2/s^2
$\overline{ED}$	non-depersonalized energy dissipation
$f(\boldsymbol{x})$	objective function
$\mathbf{F}$	body force per unit volume, $kg/(m^2 \cdot s^2)$
$\overline{g}$	minimum volume constraint
GT	geometry trimming
h	height, m
$\mathbf{I}$	identity matrix
$\mathbf{K}$	deviatoric (viscous) stress tensor, Pa
k	turbulent kinetic energy, m^2/s^2
m	mass flow rate, kg/s
$\overline{m}$	mean mass flow rate via outlets, kg/s
MF	maldistribution factor
$\overline{MF}$	non-depersonalized maldistribution factor
MUMPS	multifrontal massively parallel sparse direct solver
N_d	number of elements used for optimization
n	number of outlets
P_k	production term, $kg/(m \cdot s^3)$
p	pressure, Pa
PARDISO	parallel direct sparse solver
q	interpolation factor
Re	Reynolds number
R^2	coefficient of determination
s	distance, mm
t	time, s
TO	topology optimization
TOBS	topology optimization of binary structures
u	velocity, m/s
$\boldsymbol{u}$	velicity vector, m/s
$\overline{u}_{in}$	average inlet velocity, m/s
w	weight
x	design variable at individual grid point
$\mathbf{x}$	matrix containing design variable at all points in the mesh
X, Y, Z	Cartesian coordinate system

Greek symbols

β	element flip limit
β^*	closure coefficient
δ	diffusion tuning parameter
ε	constraint relaxation parameter
ι	convergence tolerance
μ	dynamic viscosity, $kg/(m \cdot s)$
ρ	density, kg/m^3
ω	specific turbulence rate of dissipation, 1/s
Ω	flow domain

Subscripts

0	initial value
art	artificial
f	flight
in	inlet
o	outlet
r	relative
T	turbulent

Superscripts

k	optimization iteration

One family of techniques that can assist with this manifold-optimization problem is density-based topology optimization (TO). It has the best potential to optimize as it explores the full domain and is not just dependent on the engineer's initial guess. There has been intensive work to develop this technique and to make it work with a variety of boundary conditions, especially turbulent flow.

Othmer [6] was the first to formulate a TO problem for turbulent flows. This, however, came with a caveat - their formulation neglected the variation in turbulent viscosity due to changes in the design variables, thus making the "frozen turbulence" assumption. This reduces the accuracy of the calculated sensitivities of the objective function to the various design variables. Kontoleontos *et al.* [7] corrected this by using the Spallart-Allmaras turbulence model and solving adjoint equations for it. This allowed them to correct the discrepancies in the frozen turbulence assumption. Dilgen *et al.* [8] further improved upon this by devising a method to compute the exact sensitivities *via* automatic differentiation. Their proposed technique works with a variety of closure models like k-ω and Spallart-Allmaras while being computationally cheap.

However, the density-based methods described above cannot use a discrete formulation for density. Attempting to do so typically results in "checkerboarding," where the optimizer produces extremely fine features with similarly small spaces between them. A continuous formulation is thus used, allowing for densities between 0 (fully solid) and 1 (fully liquid). This also allows for gradient-based optimization to be performed, at the cost of impacting the solution of the Navier-Stokes equations. It also results in "grayscale" areas (neither fully solid nor fluid). This is undesirable from both a manufacturing and end-use standpoint.

Fortunately, a very stable method has recently been developed with a discrete formulation for density, known as "topology optimization of binary structures" (TOBS). This method was first proposed in the structural domain by Sivapuram and Picelli [9]. Souza *et al.* [10] then applied this to flow topology optimization. Picelli *et al.* [11] then added a "geometry-trimming" (GT) procedure to the method, which

removes solid portions from the design and meshes the trimmed geometry separately. This stops flow leakage into solid regions, reduces overall domain size for faster computation, and allows for advanced meshing techniques such as mesh inflation to produce accurate results efficiently. This updated method, known as TOBS-GT, is used for this work, and will be expanded on in the following section.

Several works have investigated the use of topology optimization for manifold optimization. For example, Men *et al.* [12] optimized and investigated numerically and experimentally a multichannel heat exchanger manifold. The optimized design reduces the volume flow rate by up to 59.29% while increasing the heat transfer coefficient by 21.42% and reducing the pressure drop by 16.98% compared to the conventional rectangular header. However, most conducted studies have been focused only on a laminar flow. Similarly, as Alexandersen and Andreasen [13] note in their extensive review of literature, most optimization workflows make an extremely important assumption: optimization is typically carried out in 2D, as 3D optimization is too computationally expensive. This means the effect of the top and bottom walls is neglected.

As can be deduced from the above literature review, there are studies on manifolds optimization but they mainly limit themselves to 2D optimization [13]. Moreover, there are limited studies that experimentally validate their optimized designs [13]. Lastly, no studies compare the optimized header designs in laminar and turbulent regimes [13]. It is still unknown if the optimized manifold geometry using 2D and 3D optimization for laminar and turbulent flow is the same.

As Alexandersen and Andreasen [13] point out in their work, there is a simple solution to reduce the difference between 2D and 3D computation—incorporating the out-of-plane viscous resistance as a separate term in 2D computation. However, all but three works cited in their review fail to include this in their modeling. Therefore, one of the objectives of this work is also to examine the differences between 2D optimization, as performed in the literature, and more intensive 3D optimization.

The current study focuses on 2D and 3D optimization of inlet manifold in laminar as well as turbulent flow revealing the differences in those different approaches. Many fluid problems are solved in simple cases, but when we apply them to real-world scenarios, new issues emerge that were not apparent in the basic cases. This work explores these potential problems and solutions in the context of our industrial application.

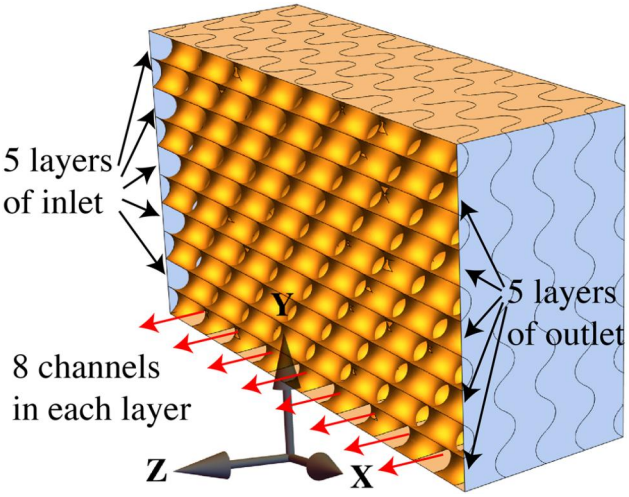

Figure 1. Schwartz diamond core considered in this work.

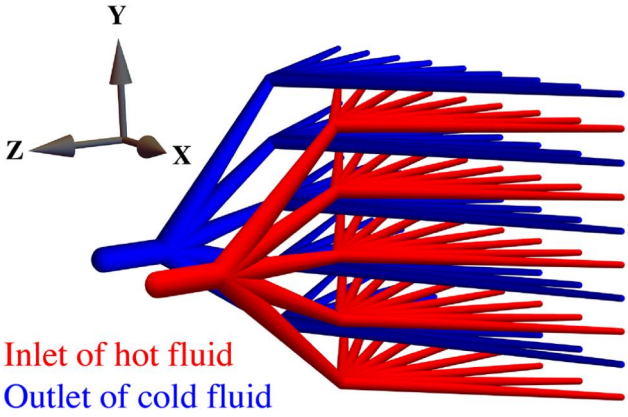

Figure 2. Schematic of inlet and outlet manifolds for the core in Figure 1.

Methodology

Geometry

The core geometry considered in this work is a "Schwartz diamond" core already optimized by a team at Université de Toulouse, in collaboration with the Total energies company. Its dimensions are $100 \times 200 \times 100$ mm, and the distribution of inlets and outlets is described in Figure 1.

In Figure 2, we see the two-stage inlet manifold that is envisaged for the core. The first stage distributes the flow from a single inlet to the five horizontal levels. The second stage distributes the flow for its respective level into eight outlets which enter the core. Only the second stage is discussed and optimized here.

Definition of maldistribution factor

While maldistribution can take several forms, in this work it is defined as differing flow rates through all

outlets of the manifold. This is quantified using a maldistribution factor (MF) as:

$$\mathrm{MF}_{\%} = \sqrt{\frac{1}{n-1}\sum_{i=1}^{n}\left(\frac{m_i - \overline{m}}{\overline{m}}\right)^2} \times 100 \qquad (1)$$

where n is the number of outlets, m_i is the mass flow rate through each outlet, and $\overline{m}$ is the mean mass flow rate through the outlets. This definition is also used in other work in literature, for example by Minqiang *et al.* [14]. Dabrowski [15] recommends this definition as it can consistently characterize the evolution of multiple properties across Reynolds numbers, indicating that it is robust.

Optimization

The TOBS-GT method follows a stepwise methodology indicated below:

1. An initial domain is fed into the optimizer, which is written in MATLAB.
2. Solid parts of the domain, if any, are removed via a GT script.
3. This trimmed geometry is then transferred to COMSOL where it is meshed.
4. The objective function and sensitivities are calculated at each point in the COMSOL mesh.
5. This information is relayed back to MATLAB and interpolated over a structured mesh used in the optimizer. The filtering is then applied.
6. The optimizer updates the geometry using Integer linear programming. This geometry is then smoothed.
7. We then return to step 2. The loop continues until convergence is reached.

This methodology is explained in further detail in the work by Picelli *et al.* [11].

Governing equations and numerical analysis

Governing equations

In this work, only incompressible flows are considered, so the fluid density does not vary across the domain. Therefore, the continuity equation can be written as:

$$\nabla \cdot \boldsymbol{u} = 0 \qquad (2)$$

COMSOL uses the Navier-stokes momentum conservation equations, which are written as:

$$\rho(\boldsymbol{u} \cdot \nabla)\boldsymbol{u} = \nabla \cdot [-p\mathbf{I} + \mathbf{K}] + \mathbf{F} \qquad (3)$$

The deviatoric stress tensor can further be expressed as:

$$\mathbf{K} = \mu(\nabla \boldsymbol{u} + \nabla \boldsymbol{u}^{\top}) \qquad (4)$$

The body force per unit volume, **F**, makes the momentum equation differentiable with respect to $\boldsymbol{x}$ and its primary purpose is to enable sensitivity calculations. It can be expanded as:

$$\mathbf{F} = -\big(q \cdot (1-x)/(q+x)\big) \cdot \boldsymbol{u} \qquad (5)$$

where q is set as 1 in our case.

The k-ω model is used as it is recommended for internal flows. It introduces additional transport equations to calculate additional variables that allow for closure of the Navier-Stokes equation. COMSOL uses the Wilcox revised k-ω model [16] which calculates k, and ω. These are calculated *via* the following equations:

$$\rho(u \cdot \nabla)k = \nabla \cdot \left[\left(\mu + \frac{\mu_{\mathrm{T}}}{2}\right)\nabla k\right] + P_k - \beta^{*}\rho\omega k \qquad (6)$$

$$\rho(u \cdot \nabla)\omega = \nabla \cdot \left[\left(\mu + \frac{\mu_{\mathrm{T}}}{2}\right)\nabla \omega\right] + \frac{13\omega}{25k}P_k - \rho\beta\omega^2 \qquad (7)$$

COMSOL automatic wall treatment is used, which employs wall functions only when the mesh near the boundary is not ideal to compute flow directly.

To aid convergence in cases where it is elusive, the strategy of inconsistent stabilization is used. To stabilize the Navier-Stokes computation, artificial diffusion is defined as follows:

$$c_{\mathrm{art}} = \delta e ||\boldsymbol{u}|| \qquad (8)$$

where e is the element size, $||\boldsymbol{u}||$ is the advection in the mesh, and δ is a tuning parameter, set as 0.25. This is added to the physical diffusion, i.e. the viscosity as $(\mu/\rho) + c_{\mathrm{art}}$. This added diffusion is isotropic, and "inconsistent" as the added diffusion remains regardless of solution accuracy. Artificial diffusion is similarly added to the turbulence equations.

For 2D CFD (computational fluid dynamics) computation, the PARADISO (Parallel Direct Sparse Solver) method was used. This is a fast and quite robust method based on lower-upper decomposition [17]. For 3D CFD computation, the MUMPS (Multifrontal Massively Parallel Sparse Direct Solver) method was used. While it is largely similar in nature to PARADISO, it also has support for cluster computing, which helps in solving larger problems with more powerful machines.

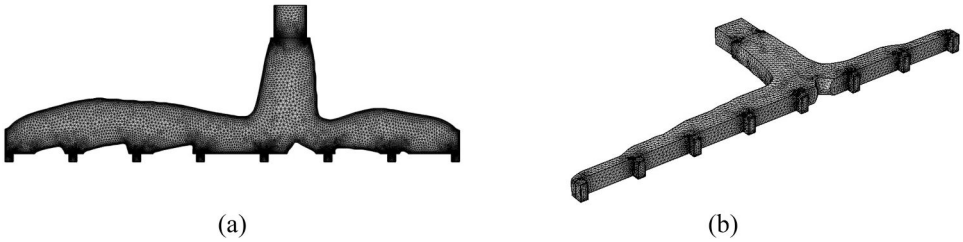

Figure 3. Selected mesh refinement levels for (a) 2D and (b) 3D flows.

Table 1. Number of elements in 2D and 3D meshes generated at each setting.

Size setting	# Elements (2D)	# Elements (3D)
Extra fine (2)	47,219.000	
Finer (3)	19,573.000	
Fine (4)	9136.000	504,887.000
Normal (5)	6488.000	200,301.000
Coarse (6)	5126.000	110,713.000
Coarser (7)	3871.000	45,990.000
Extra coarse (8)	3006.000	25,295.000
Extremely coarse (9)		12,094.000

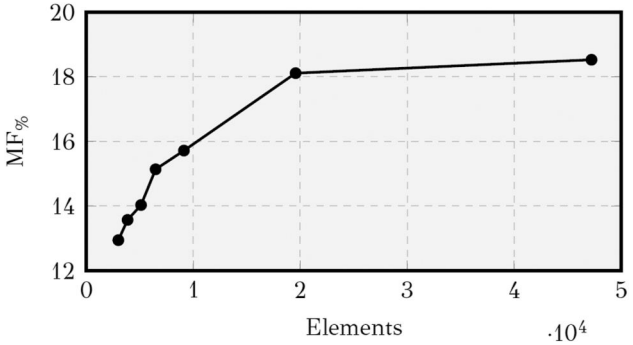

Figure 4. 2D mesh independence study (settings 2–8).

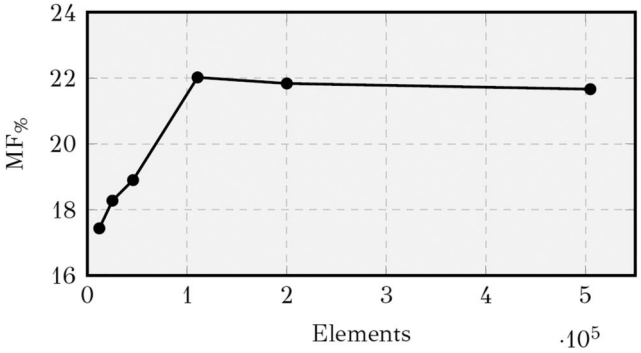

Figure 5. 3D mesh independence study (settings 4–9).

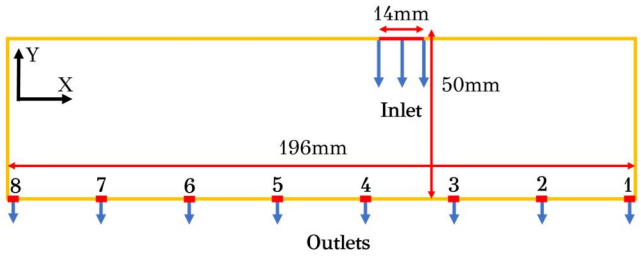

Figure 6. 2D domain used for optimization in this work.

Mesh independence

COMSOL pre-defined mesh refinement levels are used across the work to handle meshing, both during the optimization and numerical reevaluation of generated geometry. These handle various qualities such as element size, growth rate and inflation parameters automatically. This allows the meshing software to adapt with the changing geometry across iterations, avoiding the need for manual input during optimization. In the study, P1 + P1 discretization is used, which implies linear elements for both velocity and pressure calculation. This is both computationally cheap and numerically stable as it is less prone to spurious oscillations.

A 2D and 3D mesh independence check was performed on one of the optimization outputs (see Figure 3) by varying element size and observing the effect on MF. The element number for each of these sizes is given in Table 1. The "finer" (2) setting was used for 2D and "coarse" (6) for 3D. The results of the independence check are plotted in Figures 4 and 5.

Problem definition

To begin optimization, the first step is to clearly define the optimization domain and the optimization problem in a mathematical form.

Flow domain and boundary conditions

A 196mm × 50mm flow domain Ω is defined for 2D optimization (see Figure 6). The domain is rectangular to explore the optimization area as fully as possible. One inlet $\partial\Omega_{\text{in}}$ of 14mm width is prescribed, with eight outlets $\partial\Omega_{\text{out},i}$ of width 3.5 mm each on the opposing wall. For 3D optimization, the domain retains the same in-plane dimensions (196 mm × 50 mm) and includes a Z-axis height of 8 mm.

At the inlet, a fully developed velocity profile is prescribed in accordance with the Re set for optimization. This is done via the "fully developed flow" setting available in COMSOL. Instead of defining this

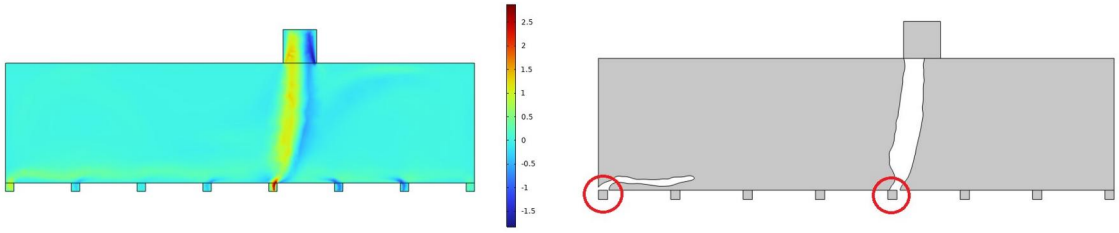

(a) Sensitivity (b) Output geometry

Figure 7. Initial sensitivity and subsequent output with MF as objective. Positive sensitivity indicates the element is preferred as a solid, and vice versa.

flow profile via an equation, this creates a virtual inlet duct. Upon the inlet of this duct, the correct amount of pressure is defined so as to produce the requested average inlet velocity at the true inlet. This average velocity is calculated from Re as:

$$\overline{u}_{in} = \frac{\mu}{\rho d_{\text{in}} Re} \tag{9}$$

where d_{in} is the width of the inlet. All outlets are set to atmospheric pressure, with walls assumed to be smooth with the no-slip condition.

Objective function

Initially, the objective function was set as minimizing the MF. The optimizer behaves as expected, with the sensitivities indicating that it intends to constrict the outlets receiving the greatest flow, as seen in Figure 7a. However, this behavior is stronger than expected and always results in one or several outlets being blocked within a single iteration, as seen in Figure 7b. Once blocked, it is difficult to unblock an outlet. This is because once regions are trimmed out by the GT algorithm, they are not evaluated for sensitivity. They are assumed to have zero sensitivity and preserve their solid state.

Therefore, a weighted objective function is devised, with $\text{MF}_{\%}$ being weighed against ED, the energy dissipation of the flow. For a 3D domain, ED can be written as:

$$\text{ED} = \mathbf{K}\nabla\boldsymbol{u} + \left(q(1-x)/(q+x)\right)\left({u_{\text{X}}}^2 + {u_{\text{Y}}}^2 + {u_{\text{Z}}}^2\right) \tag{10}$$

Since the orders of magnitude of these two objectives can be well apart, they cannot be added directly with a weight. They must therefore be nondimensionalized. For MF this is done by dividing it by the maximum possible MF achievable, i.e. in the case when only one outlet is receiving all the flow. This can be calculated using Equation (1), by setting $m_1 = 8\overline{m}$ and the rest as zero.

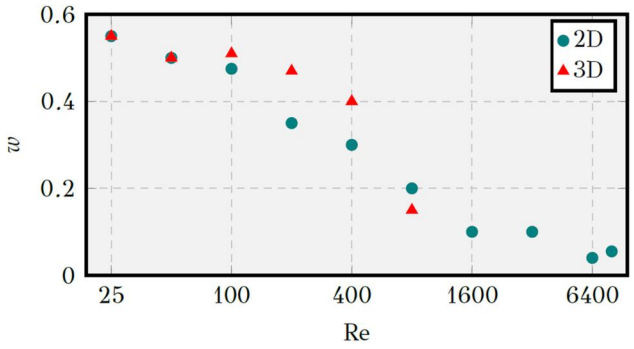

Figure 8. Variation of minimum viable weight with Re.

For ED this is done by dividing it by the value achieved in the initial domain/geometry, i.e. ED_0. The weighted and nondimensionalized objective function therefore becomes:

$$f(\boldsymbol{x}) = w \cdot \overline{\text{ED}} + (1-w)\overline{\text{MF}} = w\frac{\text{ED}}{\text{ED}_0} + (1-w)\frac{\text{MF}}{\sqrt{8}} \tag{11}$$

With w being the weight. As previously discussed, although our focus is minimizing MF, this weight cannot be set as zero or the optimizer blocks outlet(s) with the highest flow. Therefore, the value of w is chosen as the minimum with which it is possible to obtain an optimized geometry with all outlets receiving non-zero flow. Unfortunately, at present the only way to do this is tedious parameter tuning. A manifold was optimized for flows at several different Re, and the objective function was tuned by adjusting w. w was found to have a log-linear relation with Re, as illustrated in Figure 8. This means that the difficulty of optimizing for MF decreases more strongly with Re than optimizing for ED.

Constraints

With the discussion from the previous subsection, it seems logical to first implement a minimum mass-flow constraint on each outlet. However, this was

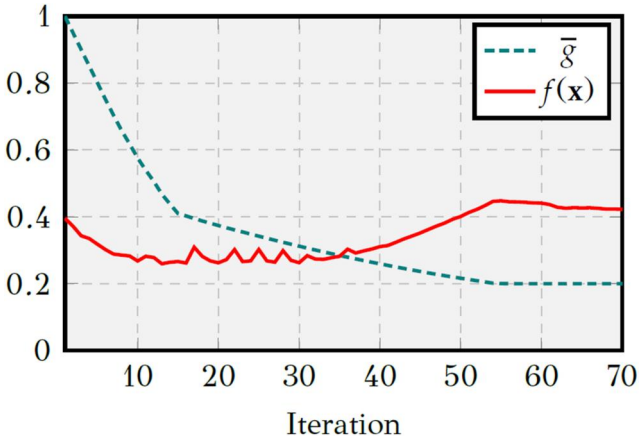

Figure 9. Optimization with $\overline{g}$ set too low.

unable to be implemented in this work for two reasons:

- For every outlet that flow is constrained for, an independent COMSOL evaluation must be performed for sensitivity to the constraint. Thus it proved prohibitive computationally, as the effort is multiplied nine times (one objective and eight constraints).
- The flow is constrained across the entire length from inlet to outlet. This often changes the optimized geometry significantly, thus having more than a merely constraining effect.

Therefore, the approach discussed in the previous section with a weighted objective function was retained. Only a minimum volume constraint, $\overline{g}$, was applied to the problem, with this volume being simply defined as the average density of elements in the domain. It was observed that the optimizer prefers reaching $\overline{g}$ over minimizing the objective, as seen in Figure 9. Therefore, $\overline{g}$ also becomes a parameter for tuning that affects the optimized output.

As observed in Figure 9, there is an inflection point where the objective is compromised with further volume reduction. The strategy chosen for picking $\overline{g}$ is then to first set it extremely low, find this inflection point, then use it to obtain a converged optimization result. While optimizing for flows at several different Re and tuning $\overline{g}$ for each, it was also found to have a log-linear relation with Re, as illustrated in Figure 10.

This implies that manifolds designed for higher Re values can be made more compact without compromising $f(\mathbf{x})$. A possible reason for this is that as inertial forces dominate over viscous ones with increasing Re, the flow "self-organizes" into narrower channels. This means a larger portion of the domain is without any flow, allowing the manifold design to exclude

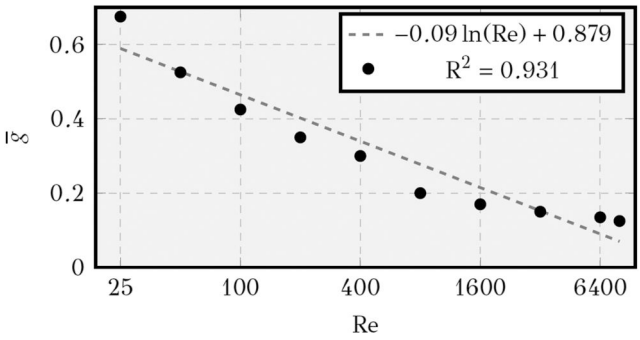

Figure 10. Variation of preferred volume constraint with Re.

Table 2. Parameters used for the TOBS-GT optimizer in the 2D domain.

Parameter	Value
Sensitivity filter radius	0.020
Density filter radius	0.040
ε	0.020
β	0.050
ι	0.001

Table 3. Parameters used for the TOBS-GT optimizer in the 3D domain.

Parameter	Value
Sensitivity filter radius	0.050
Density filter radius	0.050
ε	0.020
β	0.050
ι	0.001

most of it. This effect can be observed better in the following sections.

The parameters used in the TOBS-GT optimizer for 2D and 3D optimization are summarized in Tables 2 and 3, respectively.

The final problem definition can then be written as follows:

$$\text{Minimize } \frac{\partial}{\partial \mathrm{x}}\left(w\frac{\mathrm{ED}}{\mathrm{ED}_0}+(1-w)\frac{\mathrm{MF}}{\sqrt{8}}\right)\Bigg|_{\mathrm{x}^k}\Delta \mathrm{x}^k \tag{12}$$

$$\text{Subject to } \frac{1}{N_d}\frac{\partial\left(\sum_{i=1}^{N_d}x_i\right)}{\partial x}\Bigg|_{x^k}\Delta x^k \le \overline{g}-\frac{\left(\sum_{i=1}^{N_d}x_i\right)^k}{N_d} \tag{13}$$

and

$$\Delta x_j \in \{-x_j, 1-x_j\} j \in [1, N_d] \tag{14}$$

Experimental validation

Experimental validation was then performed to verify the $\mathrm{MF}_{\%}$ of the optimized geometry. For 2D optimization, the flow domain was converted to 3D by simply

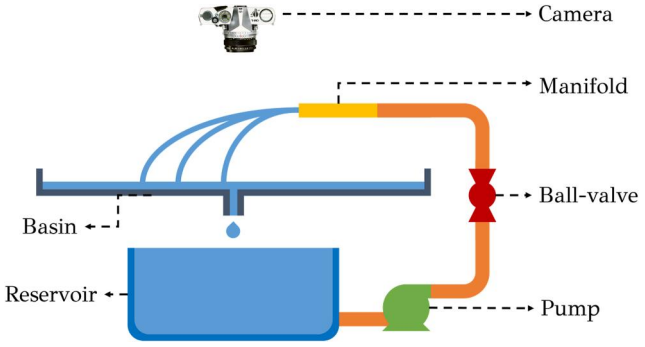

Figure 11. Experimental setup used for validation.

extruding the geometry by 8 mm. A manifold was then designed around this domain and manufactured *via* an stereolithography resin printer with a layer height of 50 microns.

A traditional means of measuring $MF_{\%}$ would be to directly measure flow from each outlet *via* a flow meter. While this would be extremely accurate, it would necessitate the connection of eight separate flow meters, one for each outlet. This is because introducing back-pressure to any one of the outlets significantly changes the pattern of flow. Therefore, flow-meters would have to be installed in every outlet simultaneously. Venturi-meters and orifice plates similarly introduce uneven back-pressures that largely neutralize the differences in outflow between each outlet.

An unorthodox method was therefore used to measure $MF_{\%}$, which will be explained in this section. The manifold is placed level at a certain height from a flat basin. Water is pumped into the manifold and allowed to freely stream out of each outlet and land on the basin. The flow from each outlet is then recorded by means of a camera and image processing. The volume of water collected in the basin is also measured to determine total flow rate and flows back into a reservoir from which it is pumped again. For more clarity, the setup is illustrated on Figure 11. The rest of this section describes the method in greater detail.

It is known, from basic kinematics, that the water exiting the outlet follows roughly the shape of a parabola. The time it remains airborne is proportional to the height of the outlet as:

$$t_f \propto \sqrt{h_o} \tag{15}$$

The horizontal distance traveled by the water while airborne is therefore proportional as:

$$s = u \cdot t_f \propto u\sqrt{h_o} \tag{16}$$

Provided the manifold is level, the height is the same for each outlet. This distance thus becomes an accurate proxy for the velocity and therefore flow rate and can be used to directly calculate $MF_{\%}$ without requiring velocity measurements.

To minimize error in practice, the camera was held at least 1.5 m above the setup with a narrower focal length of 50 mm to avoid distortion caused by wide angle lenses. Any unavoidable distortion was corrected using the respective lens profile in Adobe Lightroom. A lower shutter speed of 1/30 was also used to smooth any irregularities in the flow. *imageJ* was the software of choice for processing these images. Lengths of each outlet jet were calculated in terms of the number of pixels taken up in the image, since only the relative size of each jet is relevant for $MF_{\%}$ calculation.

Error analysis was performed on this experimental technique using the guidelines from Moffat [18]. Due to the camera resolution and image distortion, the measured mass-flow out of each individual outlet was observed to have an uncertainty of ±15%. The effect of this value on the uncertainty in MF was calculated to be 3.5%, using the equation below:

$$\delta MF_{m_i} = \frac{-\delta m_i}{14 \cdot MF \cdot m_i} = 3.5\% \tag{17}$$

We can then combine the contributions of all the outlets, to give us an error margin of ±10%, using the equations below:

$$\delta MF = \sqrt{\sum_{i=1}^{8} \delta m_i^2} = 10\% \tag{18}$$

However, laminar flow has proven challenging to validate. For the experiment to represent operation with a heat exchanger, the manifold must be full of fluid. For extremely low flow rates, this requires a certain amount of evenly-applied back-pressure. This would require the closing of the loop, which would make the chosen method difficult to apply. Therefore, only turbulent flows are validated here.

A recommendation to future users of this method would be to use more viscous alternatives to water such as oils or glycerol if validating laminar flow. This preserves the high flow rate while allowing for low Re. However, most such fluids are tedious to clean up, may require alternate pumps, and prevent the testing of turbulent flow with the same loop with water. This was therefore not attempted in this work.

Results and discussion

Optimization output

Comparing 2D and 3D simulation

The 2D simulation assumes that the domain is infinite in the precise axis where in reality the domain is

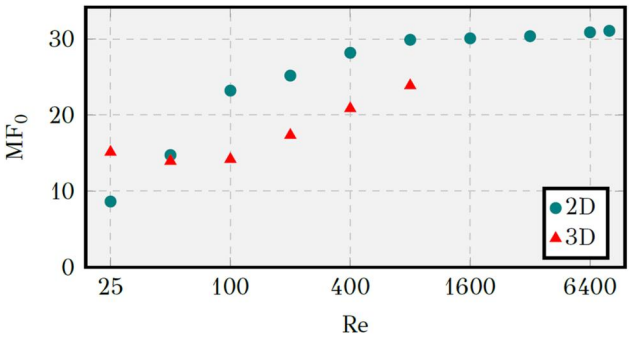

Figure 12. MF_0 inside 2D and 3D initial domains for various Re values.

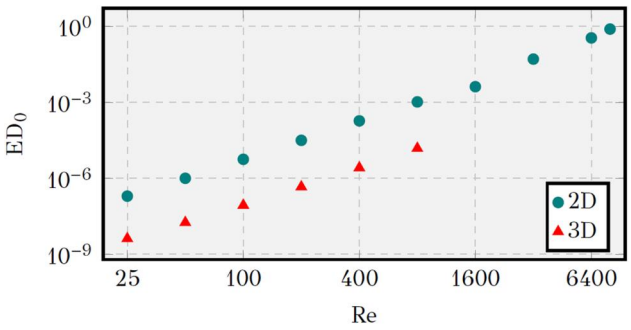

Figure 13. ED_0 inside 2D and 3D initial domains for various Re values.

thinnest. One might question then how this 2D assumption affects the outcome of optimization. In Figures 12 and 13 we can see that while the value of performance metrics differs between 2D and 3D simulation of the initial domain, their evolution with respect to Re is quite similar. The exception to this is at low Re values (25–100), where $MF_{\%}$ stays constant for the 3D case but not the 2D one.

However, in Figure 14, we can see a considerable difference in the nature of flow, especially at lower Re values between the 2D and 3D initial domain geometries. All 3D domains show negligible flow recirculation compared to the 2D ones. Comparing Figure 14a,b, it can be noted that while the former looks similar to high Re flows, in the latter the flow splits up just as it enters the domain. As we see later, this affects the design philosophy quite considerably. In contrast, the flow profile in the higher Re cases in Figure 14e,f is quite similar, save for the lack of recirculation.

As seen in Figure 15, the flow in the manifold, even at Re of 800, does not demonstrate recirculation in the YZ plane, having a largely parabolic profile. Therefore, all figures of manifolds in this work display them from the XY plane (i.e. looking down) as this is where the most interesting flow structures are observed.

Comparing 2D and 3D optimization

Trends observed in the initial domain also predictably affect the optimization output. As seen in Figure 16, 3D optimization does not consider recirculation effects during the optimization process either. Moreover, as expected, there are striking differences in the 2D and 3D-optimized geometries for low Re values, and greater similarity between the high Re designs, save for the addition of a recirculation loop. Comparing the manifolds for a Re of 50 in Figure 17a,b, we see that the former splits off far closer to the outlets than the latter. This implied that 3D optimization has value for all Re over 2D optimization. Finally, we see that the manifolds for high Re in Figure 17e,f are not only lower in volume, but closer to the outlets (and therefore the heat exchanger), making the entire assembly far more compact.

Looking at the performance of these manifolds in Figures 18 and 19, we see that $f(\mathbf{x})$ follows similar trends. Higher Re manifolds tend to distribute flow more equally, because we are able to set w lower. Overall performance, however, improves quite linearly with Re. Curiously, as opposed to Figure 12, we see that 3D-optimized manifolds appear to perform worse than their 2D-optimized counterparts. However, the 2D-optimization carries the assumption discussed in the beginning of the section—that the geometry is infinite in the Z-direction. Therefore, we can reason that if the 2D geometry were extruded in the Z-direction and evaluated in a 3D solver, it would perform worse than the respective 3D optimized design.

Lastly, the optimized manifolds are compared to the initial domain by plotting relative values for MF and $f(x)$, which can be defined as:

$$\mathrm{MF_r} = \frac{\mathrm{MF}}{\mathrm{MF_0}} \tag{19}$$

$$f(\boldsymbol{x})_\mathrm{r} = \frac{f(\boldsymbol{x})}{f(x)_0} \tag{20}$$

This information, in Figures 20 and 21, allows us to track the optimization process at each Re. The lower MF_r and $f(\mathbf{x})_r$ the more effective the optimization has been. This reveals something interesting—in 2D optimization, performance improves over the initial domain for all Re, but 3D optimization reveals that performance improves only for the high Re manifolds. Therefore, for lower Re, there is in actuality a tradeoff between performance and compactness, while 2D optimization results would have us believe otherwise.

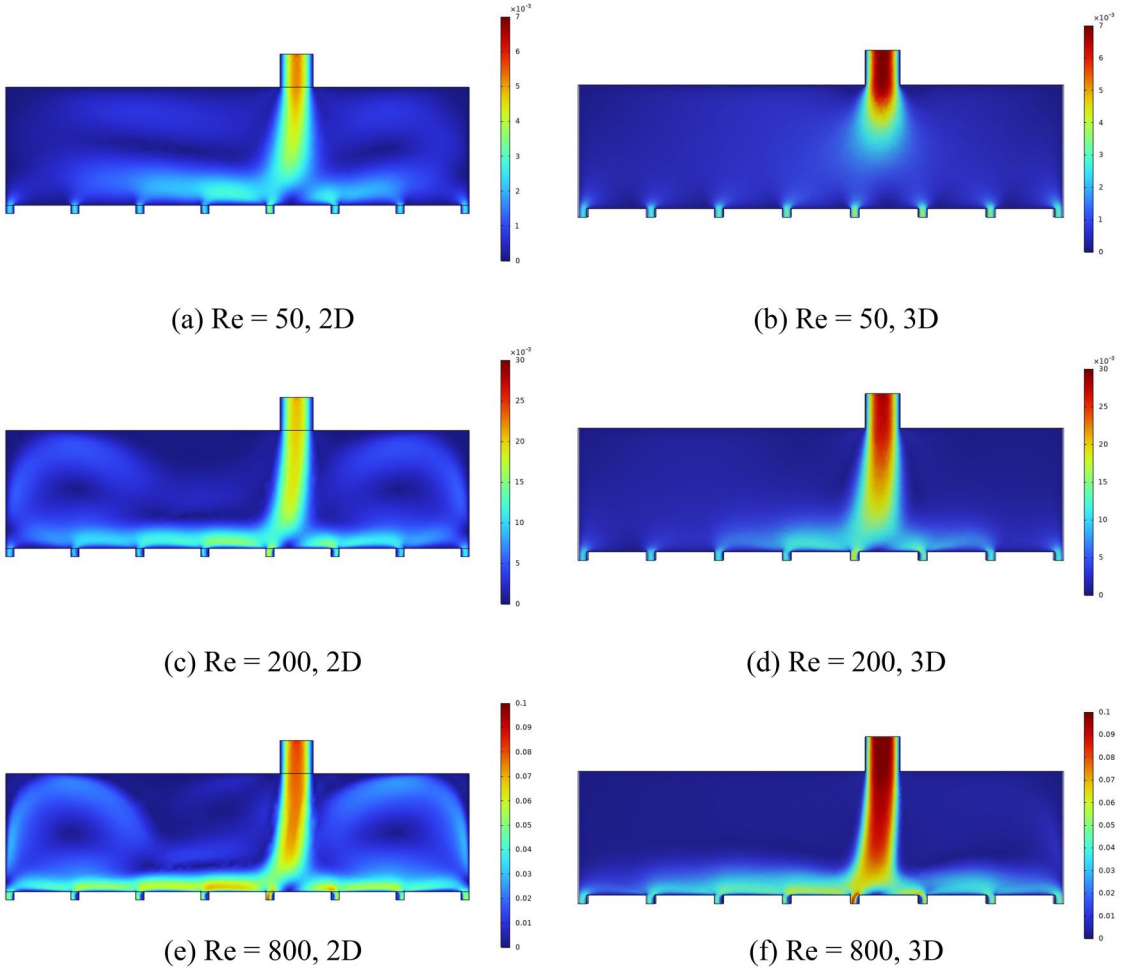

Figure 14. Comparison of velocity contours (m/s) in the initial domain.

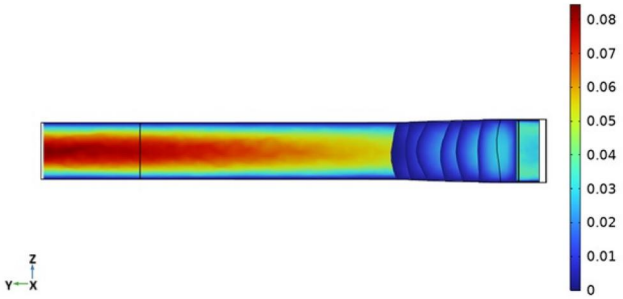

Figure 15. Velocity (m/s) across manifold optimized at a Re of 800, seen from the YZ plane. Flow enters from the inlet on the left and leaves from the outlets on the right.

Comparing laminar and turbulent optimization

Due to the high computational requirements of 3D turbulent flow optimization, it could not be attempted in this work. The rest of this section describes the comparison between 2D laminar and 2D turbulent flow optimization.

The trend of lowering $f(\mathbf{x})$ continues with the onset of turbulence. This is likely because of turbulent flow mixing, which helps distribute the flow evenly across multiple outlets. Optimization was then performed for an inlet Re of 8000. Two geometries, illustrated in Figure 22, were produced - one by driving the weight and volume as low as possible, and another with more conservative specifications. Their performance is tabulated in Table 4.

Comparing Figures 17e and 22a, the turbulent manifold is a gradual evolution of the laminar designs for high Re.

Comparing to Figure 22a, the extreme geometry is more compact, and also lacks the separate loop seen in the conservative design, which is hard to manufacture. However, the effect of reducing w is that ED rises considerably, to about double that of the conservative design. This means that while the extreme manifold distributes flow better, pressure drop is far higher.

Despite all the optimization that has been performed in this work, it is possible that the performance improvement of the high Re geometries over the low Re designs is marginal. To rule out this possibility, the low Re optimized designs were tested for flow

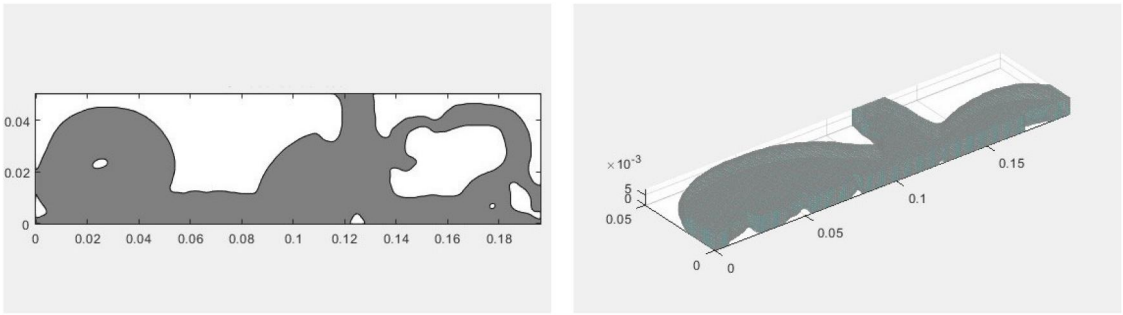

(a) 2D (b) 3D

Figure 16. Comparison of 2D and 3D optimization with an inlet Re of 800 at the 15th iteration.

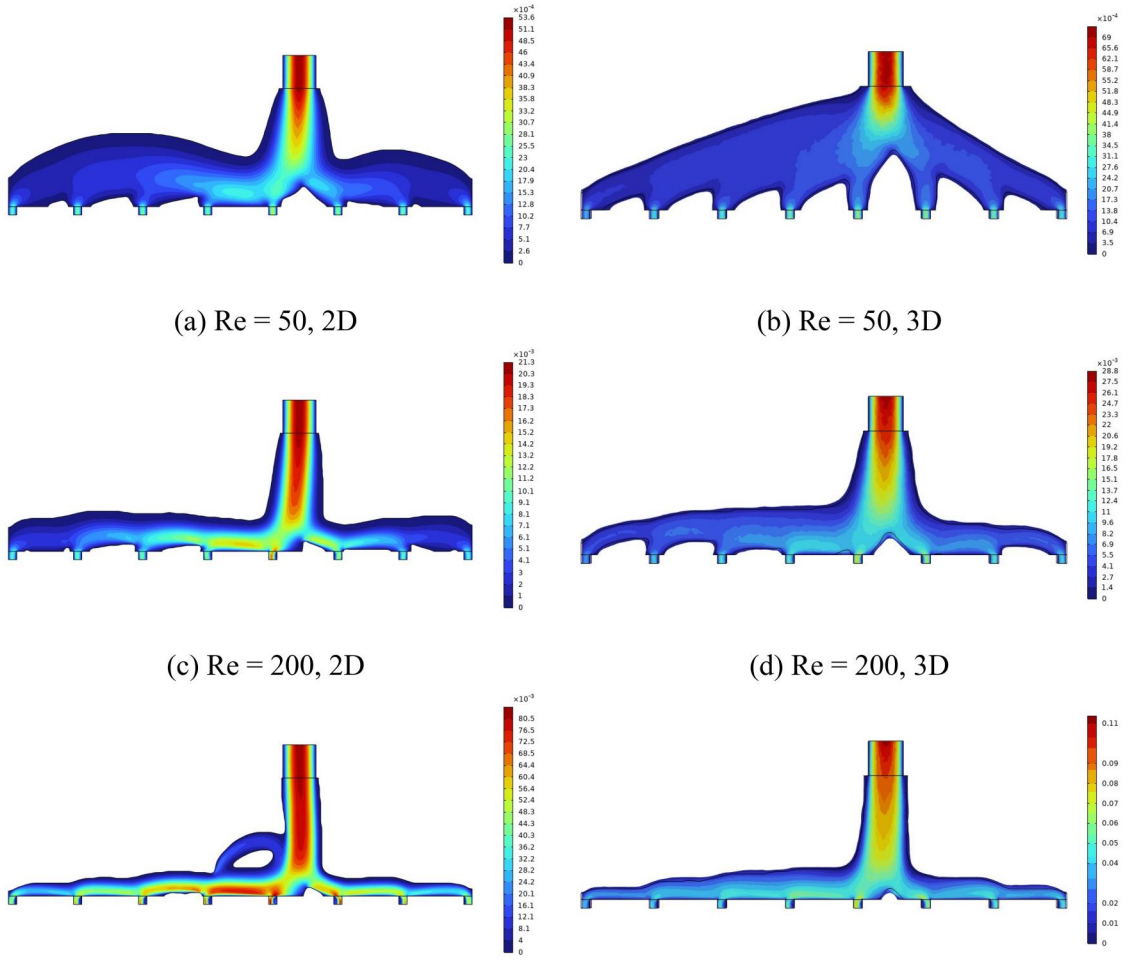

(a) Re = 50, 2D (b) Re = 50, 3D

(c) Re = 200, 2D (d) Re = 200, 3D

(e) Re = 800, 2D (f) Re = 800, 3D

Figure 17. Comparison of velocity contours (m/s) in the TO geometry.

at the highest inlet Re of 8000, and the comparison of $MF_{\%}$ can be seen in Figure 23.

It is observed that the manifolds under-perform not only compared to the manifold specifically optimized for a Re of 8000 but also compared to their own performance at their respective design Re value. This can also be observed in the flow contours within the design (see Figure 24), which shows the poor distribution quite visually. The manifold performance improves almost uniformly as the Re of optimization approaches the Re of operation.

Experimental validation

Physical models of the manifolds were produced with a two-part design: a resin 3D-printed bottom

section and a laser-cut top plate. Using the method described previously, the two geometries specifically designed for a Re of 8000 were validated. Throughout the process, validation has been tricky to achieve.

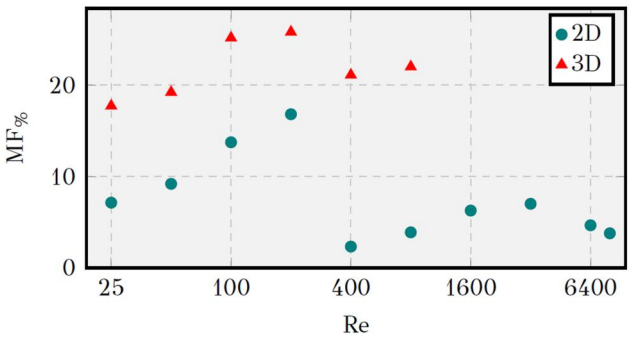

Figure 18. $MF_{\%}$ inside 2D and 3D optimized geometry for various Re values.

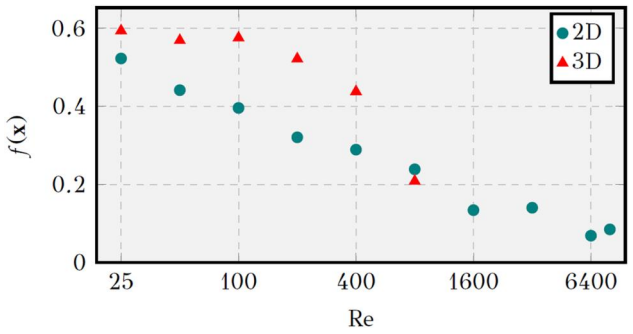

Figure 19. $f(\mathbf{x})$ for 2D and 3D optimized geometry for various Re values.

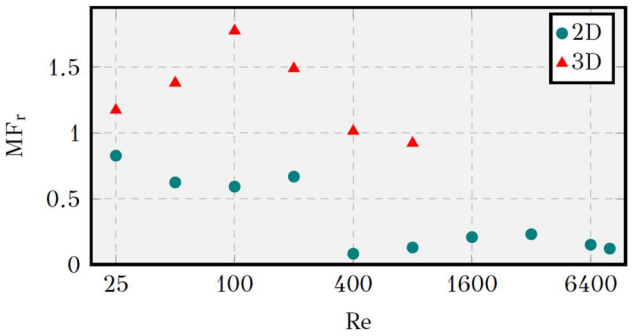

Figure 20. MF_r for various Re values.

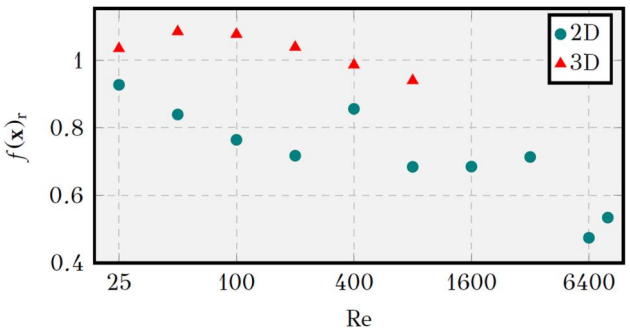

Figure 21. $f(\mathbf{x})_r$ for various Re values.

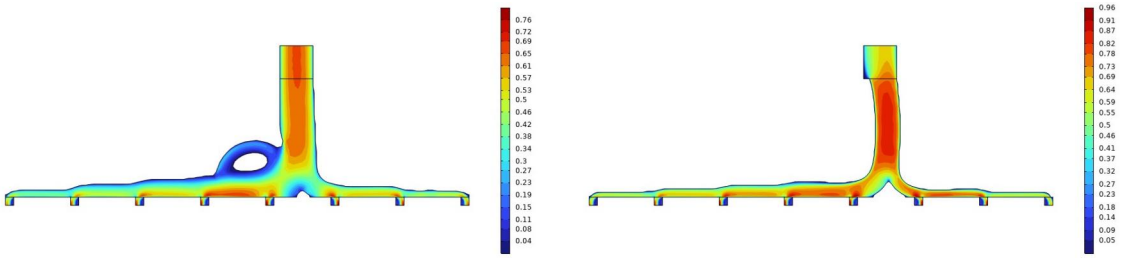

(a) w=0.1, $\bar{g}$=0.2 (b) w=0.055, $\bar{g}$=0.125

Figure 22. Velocity contours (m/s) in manifolds designed with (a) more conservative and (b) extreme values using TOBS-GT for Re = 8000.

Topology-optimized turbulent flow manifold with conservative parameters

As seen in Figures 25 and 26, this design is validated - the final value of the $MF_{\%}$ for the 3D CFD model is within the experimental error range and the flow patterns also match. The same outlets are preferred in the CFD and experimental case. An expected result is that 2D model not only fails validation quantitatively due to the disparity between $MF_{\%}$ values, but also qualitatively as the flow patterns do not match as closely. This suggests that the behavior used by the 2D optimizer of using flow recirculation zones is perhaps nonphysical.

Topology-optimized turbulent flow manifold with extreme parameters

The extreme design was not successfully validated, as seen in Figures 27 and 28. The disparity between the 3D CFD and experimental $MF_{\%}$ value is too great, even though there is a similarity between the outlet flow patterns. We do see again the trend here for 2D results to be more different both numerically and qualitatively.

Validation work shows us that it is difficult to produce optimized geometry that works just like its CFD model. There are some potential reasons these models are troublesome to validate:

- Optimization and CFD modeling were done with the assumption of fully developed flow at the inlet. For this condition to be realized in practice, there needs to be a development region of at least 10 times the inlet width [19]. Not only is this condition not satisfied in experimental validation due to the dimensions of the 3D printer, but it might also not be satisfied in operation. As seen in Figure 2, the first stage is likely to affect the inlet boundary condition for the manifold in the second stage, which might not be fully developed.
- The roughness of a 3D-printed design has not been considered during optimization, which assumes smooth walls. Especially for turbulent flow, this may also affect the result. The roughness

Table 4. Performance of manifolds designed using TOBS-GT for Re = 8000.

Variable	Conservative design	Extreme design
$MF_{\%}$	7.429	3.778
ED	2.957×10^{-4}	5.939×10^{-4}
$f(\mathbf{x})$	0.024	0.013

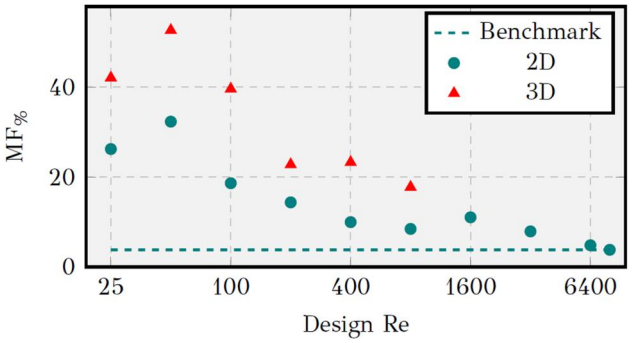

Figure 23. $MF_{\%}$ of manifolds optimized for other Re values benchmarked against the one optimized for a Re of 8000.

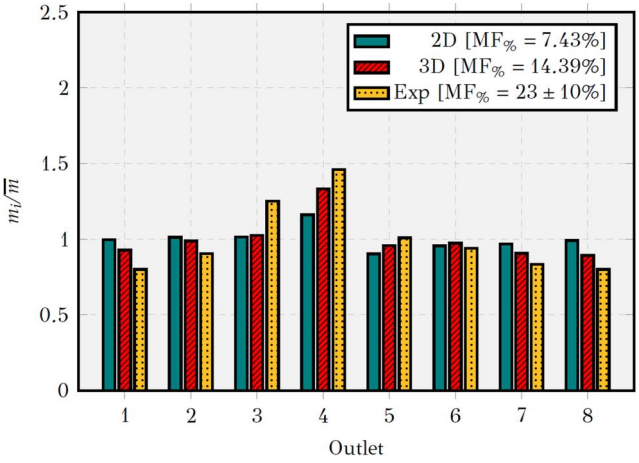

Figure 25. A comparison of the 2D and 3D models of manifold optimized for a Re of 8000 with conservative parameters with experimental validation.

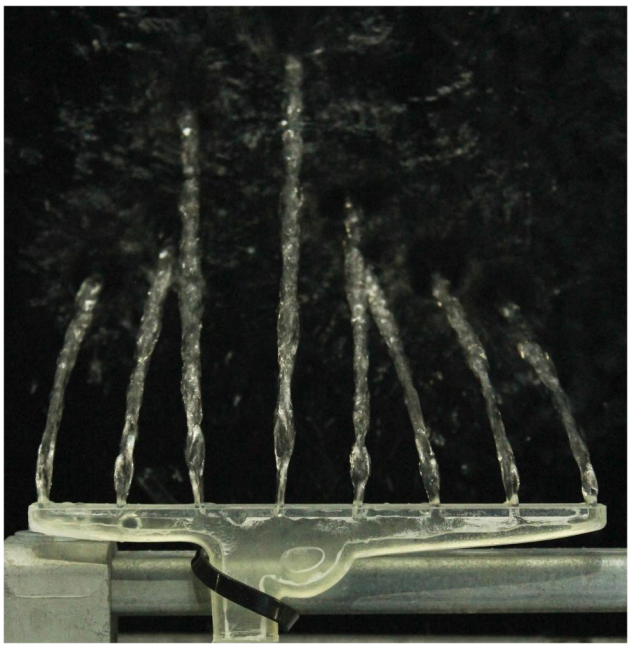

Figure 26. Image used for experimental validation of the 2D manifold optimized for a Re of 8000 with conservative parameters.

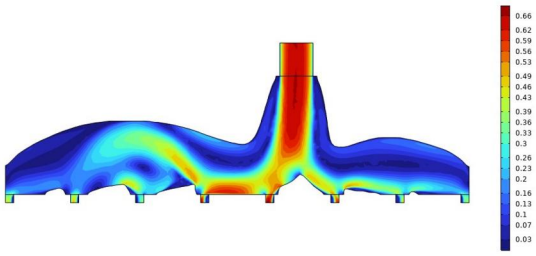

(a) Re = 50, 2D

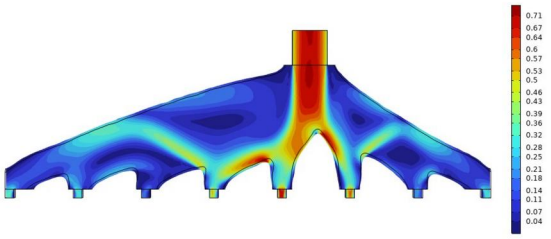

(b) Re = 50, 3D

Figure 24. Velocity contours (m/s) in manifolds designed for low Re being used for a Re of 8000.

characteristics are also likely to be different for the resin-printed prototype, and the metal-printed final design.

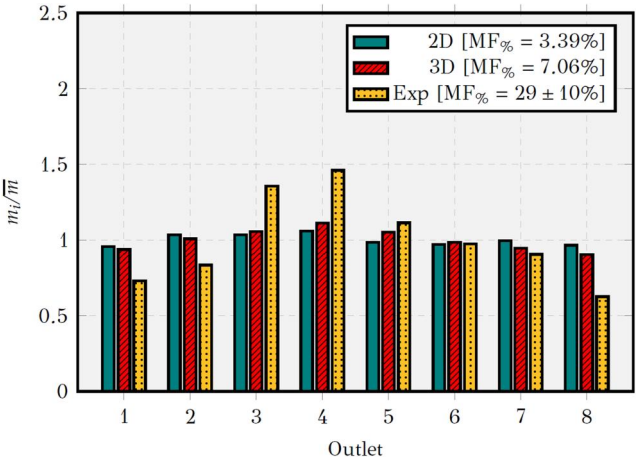

Figure 27. A comparison of the 2D and 3D models of manifold optimized for a Re of 8000 with extreme parameters with experimental validation.

Conclusions

The following conclusions were reached over the course of this work:

- Optimization must be done for the exact boundary conditions under which the part is expected to operate. A manifold optimized for laminar flow cannot be expected to perform well with turbulent flow.
- With the chosen optimization methodology and maldistribution definition, manifolds optimized for turbulent flow achieve better flow distribution than ones designed for laminar flow at their respective design conditions.
- Manifolds designed for higher Reynolds numbers also achieve a more compact design without compromising the flow distribution. This geometry not only has lower volume overall but is closer to the outlets, thus producing a compact heat exchanger overall.

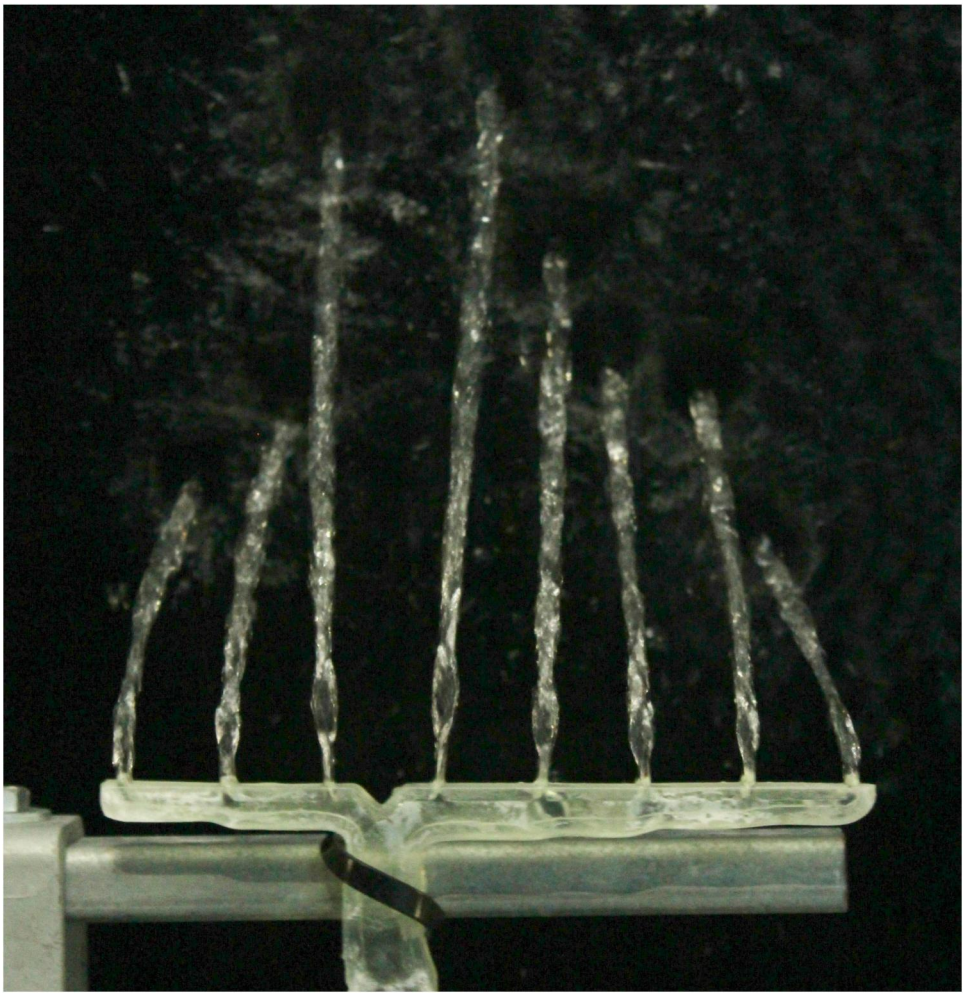

Figure 28. Image used for experimental validation of the 2D manifold optimized for a Re of 8000 with extreme parameters.

- Where laminar flow (especially at lower Reynolds numbers) is expected, it is worthwhile to optimize with a 3D domain, despite the expected increase in computational cost. In these cases, the top and bottom wall have a strong effect on the final optimized design.
- 3D optimization is also recommended for higher Reynolds numbers. The 2D optimizer tends to overvalue the influence of recirculation effects, thus adding tough-to-manufacture yet useless loops to the manifold design.

Recommendations

The following recommendations can be made for future investigation based on the limitations of this work:

- The inlet boundary condition for the second stage can be studied by conducting CFD and validation of the first stage. This will make the optimization process more reflective of real operating conditions.
- As mentioned, roughness could not be faithfully modeled in this work and might well disrupt the flow for metal-printed parts. A potential project could physically characterize, then model, and finally optimize with the roughness of a physical metal 3D-printed part.
- An exploration of 3D turbulent optimization can show whether the trends identified with increasing Reynolds numbers for differences between 2D and 3D optimization can be extended for turbulent flow. With the non-linear nature of the transition to turbulence, this is not guaranteed.

Acknowledgements

This work would not have been possible without Dr. Renato Picelli and Lucas Oliveira, who helped us understand their TOBS optimization method and apply their optimizer code to our problem. We also thank Dr. Pawel Dabrowski, who helped refine the manuscript for submission.

Disclosure statement

No potential conflict of interest was reported by the author(s).

Notes on contributors

Mayank Kumar Gupta is a PhD candidate at the Process & Energy department at TU Delft, with a focus on high temperature heat pumps. He has previously worked on high performance heat transfer systems, in applications such as computing and nuclear fusion.

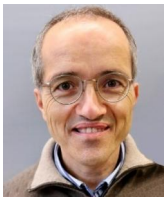

Lionel Arnaud is a university professor at UTTOP (University of Technology of Tarbes Occitanie Pyrénées, France), leading a research team and a platform on metal additive manufacturing. He is particularly interested in the links between design (notably topological optimization), the process, and the durability of parts manufactured by laser powder bed fusion.

Kamel Hooman studied and worked at The University of Queensland (Australia) before joining TUDelft as a Professor and Chair of Heat Transformation Technology in 2022. He conducts fundamental and applied research using a combination of numerical, experimental, and theoretical techniques. His work was rewarded by industry and funding agencies in Australia and overseas. He received several grants, awards, and fellowships from different agencies including The Australian Research Council and Australian Academy of Science. He was named Australian Research Field Leader in the field of Thermofluids. He serves as an Associate Editor for several journals. He chaired and organized an IAHR international conference on heat exchangers and cooling towers in Australia while serving on many international conference committees. He had visiting positions in Poland, China, Germany, Malaysia, Italy, and France. He co-edited two books on convection in porous media and thermal energy storage, both published by CRC. He has contributed to many books through chapters and published over 200 papers in international journals while delivering over 50 invited conference plenary and keynotes in US, EU, and Asia.

References

[1] A. Koca, C. İ. Çalışkan, E. Koç, and Ö. Akbal, "A novel 3D printed air-cooled fuel cooler heat exchanger for aviation industry," *Heat Transf. Eng.*, vol. 44, no. 15, pp. 1350–1371, 2023. DOI: 10.1080/01457632.2022.2134077.

[2] L. Chai and S. A. Tassou, "Recent progress on high temperature and high pressure heat exchangers for supercritical CO_2 power generation and conversion systems," *Heat Transf. Eng.*, vol. 44, no. 21–22, pp. 1950–1968, 2023. DOI: 10.1080/01457632.2022.2164683.

[3] J. Wen and Y. Li, "Study of flow distribution and its improvement on the header of plate-fin heat exchanger," *Cryogenics*, vol. 44, no. 11, pp. 823–831, Nov. 2004. DOI: 10.1016/j.cryogenics.2004.04.009.

[4] K. Zhang, M.-J. Li, H. Liu, J.-G. Xiong, and Y.-L. He, "A general and rapid method to evaluate the effect of flow maldistribution on the performance of heat exchangers," *Int. J. Therm. Sci.*, vol. 170, pp. 107152, Dec. 2021. DOI: 10.1016/j.ijthermalsci.2021.107152.

[5] P. R. Bobbili, B. Sunden, and S. K. Das, "An experimental investigation of the port flow maldistribution in small and large plate package heat exchangers," *Appl. Therm. Eng.*, vol. 26, no. 16, pp. 1919–1926, Nov. 2006. DOI: 10.1016/j.applthermaleng.2006.01.015.

[6] C. Othmer, "A continuous adjoint formulation for the computation of topological and surface sensitivities of ducted flows," *Numer. Methods Fluids*, vol. 58, no. 8, pp. 861–877, Mar. 2008. DOI: 10.1002/fld.1770.

[7] E. A. Kontoleontos, E. M. Papoutsis-Kiachagias, A. S. Zymaris, D. I. Papadimitriou, and K. C. Giannakoglou, "Adjoint-based constrained topology optimization for viscous flows, including heat transfer," *Eng. Optimiz.*, vol. 45, no. 8, pp. 941–961, 2013. DOI: 10.1080/0305215X.2012.717074.

[8] C. B. Dilgen, S. B. Dilgen, D. R. Fuhrman, O. Sigmund and B. S. Lazarov, "Topology optimization of turbulent flows," *Computer Methods Appl. Mech. Eng.*, vol. 331, pp. 363–393, Apr. 2018. DOI: 10.1016/j.cma.2017.11.029.

[9] R. Sivapuram and R. Picelli, "Topology optimization of binary structures using integer linear programming," *Finite Elements Anal. Des.*, vol. 139, pp. 49–61, Feb. 2018. DOI: 10.1016/j.finel.2017.10.006.

[10] B. C. Souza *et al.*, "Topology optimization of fluid flow by using integer linear programming," *Struct. Multidisc. Optim.*, vol. 64, no. 3, pp. 1221–1240, May 2021. DOI: 10.1007/s00158-021-02910-6.

[11] R. Picelli *et al.*, "Topology optimization of turbulent fluid flow via the TOBS method and a geometry trimming procedure," *Struct. Multidisc. Optim.*, vol. 65, no. 1, pp. 34, Jan. 2022. DOI: 10.1007/s00158-021-03118-4.

[12] Z. Men, W. Chen, Q. Hu, and S. Liu, "Numerical and experimental investigation of a multi-channel heat sink distribution header designed by topology optimization," *Appl. Therm. Eng.*, vol. 238, pp. 122008, Feb. 2024. DOI: 10.1016/j.applthermaleng.2023.122008.

[13] J. Alexandersen and C. S. Andreasen, "A review of topology optimization for fluid-based problems," *Fluids*, vol. 5, no. 1, pp. 29, Mar. 2020. DOI: 10.3390/fluids5010029.

[14] P. Minqiang, Z. Dehuai, T. Yong, and C. Dongqing, "CFD-based study of velocity distribution among multiple parallel microchannels," *J. Comput.*, vol. 4, no. 11, pp. 1133–1138, Nov. 2009. DOI: 10.4304/jcp.4.11.1133-1138.

[15] P. Dabrowski, "Comparison of various flow maldistribution quantification methods in mini heat exchangers," *Sci. Rep.*, vol. 13, pp. 11482, Jul. 2023. DOI: 10.1038/s41598-023-38784-5.

[16] D. C. Wilcox, *Turbulence Modeling for CFD*. La Canada: DCW Industries, Inc., 1994,

[17] COMSOL, "Comsol multiphysics documentation." COMSOL, Burlington, MA, USA, Nov. 2023. [Online]. Accessed: Nov. 7, 2023. Available: https://doc.comsol.com/6.2/docserver/!/com.comsol.help.comsol/helpdesk/helpdesk.html.

[18] R. J. Moffat, "Describing the uncertainties in experimental results," *Exp. Therm. Fluid Sci.*, vol. 1, no. 1, pp. 3–17, Jan. 1988. DOI: 10.1016/0894-1777(88)90043-X.

[19] Y. A. Çengel and J. M. Cimbala, *Fluid Mechanics: Fundamentals and Applications*, 4th ed. New York, NY: McGraw-Hill Education, 2018,